Journal of Catalysis 416 (2022) 311–321

Contents lists available at ScienceDirect

Journal of Catalysis

journal homepage: www.elsevier.com/locate/jcat

Improving the ORR performance by enhancing the Pt oxidation resistance

Ruoyu Xu [a,1], Liqun Kang [a,1], Konstantinos G. Papanikolaou [a], Bolun Wang [a], Sushila Marlow [a], Qian He [b], Peng Zhang [c], Jianfang Wang [d], Dan J.L. Brett [a], Michail Stamatakis [a], Feng Ryan Wang [a,*]

[a] Department of Chemical Engineering, University College London, London WC1E 7JE, United Kingdom
[b] Department of Materials Science and Engineering, National University of Singapore, Singapore 117575, Singapore
[c] Department of Chemistry, Dalhousie University, Halifax, Nova Scotia B3H 4R2, Canada
[d] Department of Physics, The Chinese University of Hong Kong, Shatin, Hong Kong Special Administrative Region

ARTICLE INFO

Article history:
Received 27 July 2022
Revised 23 October 2022
Accepted 26 October 2022
Available online 7 November 2022

Keywords:
Oxygen reduction reaction
Electron microscopy
X-ray absorption spectroscopy
Density functional calculations

ABSTRACT

Proton exchange membrane fuel cells require oxygen reduction catalysts with high activity and stability. Pt based alloy materials are most widely applied ORR catalyst due to its high intrinsic activity, but usually suffer from rapid deactivation as a result of particle agglomeration, detachment, Ostwald ripening and/or Pt dissolution. Here we investigate the degradation of the PdPt alloys *via in situ* X-ray absorption fine structure, $\Delta\mu$ analysis, identical location-electron microscopy and DFT calculations. We conclude that the origin of high activity and stability of the PdPt catalyst stems from the oxidation resistance of metallic Pt, forming mainly surface adsorbed O species at high potentials. Two stage degradation process are observed, showing an evolution of dynamic surface dependent ORR performance along with the deactivation process. The careful design of Pt alloy structure leads to controlled surface oxygen behaviours. This opens a new way to increase the lifespan of fuel cells and improve the Pt utilization efficiency.

1. Introduction

High mass activity (MA) and good stability at high potentials are the major objectives in developing new oxygen reduction reaction (ORR) catalysts for proton exchange membrane fuel cells [1-6]. Colloidal Pt alloys, such as PdPt, PtNi and PtCo, have been widely reported over the past decade for their exceptional ORR mass activity. This superior performance can be rationalized by the electronic structure of these materials and induced particle strain effect [7-13]. Their design routes for achieving exceptional ORR activities include: 1) increasing the intrinsic activity of Pt by alloying with other metals [14-18]; 2) exposing particular active lattice planes on the surface [17,19,20] and 3) improving Pt utilization *via* the deposition of Pt as ultrathin layers on suitable substrates [19,21-25]. Based on these literatures, Pt alloys have been widely reported with higher ORR activity than pure Pt catalysts [26-28].

With the current success of colloidal Pt alloys in ORR, it is important to understand the promotion role of the second metal in the stability of the alloys under acidic reaction conditions. In general, introduction of second metal tunes the oxygen adsorption energy ($E_{ads}O$) on the Pt surface, while the ORR activity is maximized when the $E_{ads}O$ is ca. 0.2 eV higher than that on the pure Pt(111) surface ($E^{Pt}_{ads}O$) [29,30]. Studies in relations to the morphology [31-34], element content [35,36] and atomic structure changes [37-39] of Pt or Pt-based alloy nanoparticles during electrochemical deactivation have revealed four main deactivation causes: (1) particle agglomeration; (2) particle detachment; (3) Ostwald ripening and (4) metal dissolution [40]. Particle agglomeration and detachment are size dependent, whereas Ostwald ripening and metal dissolution are affected by the tendency of Pt oxidation at high potentials. It is therefore important to elucidate the rational between $E_{ads}O$/surface oxygen species and the activity/stability of the Pt alloy catalysts. In particular, the dynamic alloy structure during ORR cycling will changes the surface $E_{ads}O$ and thus revealing the dynamic change of ORR activity. Understanding such dynamic is key for materials innovations with high durability and stability.

Here a PdPt alloy with unique porous structure is designed to address the deactivation causes mentioned above. It is worth mention that not only such PdPt alloy exhibits much higher mass activity than commercial Pt (0.82 $A{\cdot}mg^{-1}_{Pt}$ vs 0.13 $A{\cdot}mg^{-1}_{Pt}$), but its stability also outperforms most reported Pt-based alloy catalysts [7,19,41,42], showing only 1% MA decay in 20,000 accelerated

* Corresponding author.
E-mail address: ryan.wang@ucl.ac.uk (F.R. Wang).
[1] These authors contributed equally to this work.

https://doi.org/10.1016/j.jcat.2022.10.025
0021-9517/

durability test (ADT) cycles. The investigation of the reaction behaviour of PdPt alloy by *in situ* X-ray absorption fine structure (XAFS) study reveals that PdPt alloy is more resistant to oxidation at high potentials than commercial Pt. On top of this, $\Delta\mu$ analysis shows predominant adsorbed O on Pt surface (1-fold atop site) for PdPt alloy at high potentials, whereas the pure Pt surface prefers O insertion into the lattice, forming PtO_x (n-fold sites). Such enhanced oxidation resistance improves both the ORR mass activity and stability significantly. As a net result, the leaching of Pt from PdPt alloy only take places after 30,000 accelerated durability test (ADT) cycles. This is witnessed both at the single particle level with identical location-electron microscopy (IL-EM) [40] and ensemble level *via* microwave plasma-atomic absorption spectroscopy (MP-AES) analysis. Based on the attained PdPt alloy structure evolution, we perform periodic DFT calculations [29], showing the trend of $E_{ads}O$ along with the change of surface structure, resembling the similar trend of MA in the experiments. The presence of Pd in the subsurface layer of the PdPt alloy makes oxygen-binding less exothermic by 0.04 eV per O atom as compared to a pure Pt catalyst, suggesting the best activity among all structures. By tracing dynamic structural evolution of PdPt alloy during degradation in both theory and experiment, an accurate structure-performance relationship during the degradation of the PdPt catalysts is established with the surface oxygen adsorption as the driving force. This result is only possible with the combination of calculation, single particle and ensemble techniques, which can be widely applied for catalysis and energy applications.

2. Experimental section

2.1. Catalysts preparation

Dihydrogen tetrachloropalladate solution (H_2PdCl_4, 0.01 mol·L^{-1}, 100 mL) was prepared by dissolving palladium (II) chloride ($PdCl_2$, 180 mg, ≥99%) and hydrochloric acid (200 μ L) in water (100 mL). The obtained solution was then stirred and heated at 60 °C until it became homogeneous. Chloroplatinic acid hexahydrate solution (H_2PtCl_6, 0.01 mol·L^{-1}, 100 mL) was prepared by dissolving chloroplatinic acid hexahydrate (H_2PtCl_6, 520 mg, ACS reagent, ≥ 37.5% Pt basis) in deionized water (100 mL, 18 MΩ/cm). The PdPt/C colloidal nanoparticles were synthesized by a typical seed mediated growth method. For the preparation of the seed solution, hexadecyltrimethylammonium chloride ($C_{19}H_{42}$-CIN, ≥99%, CTAC, 12.5 mL), dihydrogen tetrachloropalladate solution (H_2PdCl_4, 0.01 mol·L^{-1}, 2.5 mL), sodium borohydride solution ($NaBH_4$, ≥98.0%, 0.1 mol·L^{-1}, 6 mL) and deionized water (85 mL) were added into a vial (volume:150 mL). After the vial had been capped, the mixture was ultrasonicated for around 30 min. The resulting homogenous seed solution was stranded at room temperature for 3 h. For the synthesis of the PdPt/C colloidal solution, chloroplatinic acid hexahydrate solution (H_2PtCl_6, 0.01 mol·L^{-1}, 8 mL), dihydrogen tetrachloropalladate solution (H_2-$PdCl_4$, 0.01 mol·L^{-1}, 8 mL), porous carbon powder (Ketjenblack EC300J, 40 mg), hexadecyltrimethylammonium chloride ($C_{19}H_{42}$-CIN, 2.4 mL), L-ascorbic acid ($C_6H_8O_6$, 4 mL) and obtained seed solution (100 mL) were added into an round bottom flask (volume: 1 L). The mixture was ultrasonicated for 30 min. The resulting homogenous mixture was then heated to 60 °C for 4 h. The resulting colloidal products were collected by centrifugation, washed three times with an ethanol/water (volume ratio 1:1) mixture and dried in oven at 60 °C. Before the electrochemistry measurements, the PdPt/C powder was washed by mixture of water and ethanol three times to remove surfactant (CTAC). There is no extra treatment for porous carbon support. Based on the MP-AES results, the weight percent of Pt and Pd is 15 wt% and 12 wt%, respectively.

2.2. Electrochemical measurement

For the ink preparation, the PdPt/C (2 mg) was dispersed in the mixture containing ethanol and Nafion (0.01 wt% Nafion, 1 mL) and then sonicated in ice bath for 30 min. Based on the MP-AES results, the total metal loading of both PdPt/C and commercial Pt/C (JM, 40 wt%, 2–5 nm Pt nanoparticles) catalyst on the glassy-carbon (GC) electrode were controlled to be 5.2 μg. All electrochemical measurements were carried by the Gamry Interface 1010E potential station using a GC rotating disk electrode (RDE, Pine Research Instrumentation, area 0.196 cm^2) connected to a rotating electrode speed control (Pine Research instrumentation). A Pt wire (99.999%) and a silver/silver chloride electrode (Ag/AgCl) were used as counter and reference electrodes. The Ag/AgCl reference electrode was calculated, which has an overpotential of +0.265 V relative to reversible hydrogen electrode (RHE) in 0.1 M $HClO_4$ electrolyte (Supplementary Fig. S27). The electrochemically active surface area (ECSA) was determined by integrating the hydrogen adsorption charge on the cyclic voltammetry (CV) curves at room temperature in N_2-saturated 0.1 M $HClO_4$ solution with a scan rate of 20 mV/s. Oxygen reduction reaction (ORR) measurements were carried in 0.1 M $HClO_4$ solution purged with saturated O_2 during the measurements. The scan rate and rotation speed for the ORR measurements were 20 mV/s and 1600 rpm, respectively. For the ORR polarization curves, the current densities were normalized in reference to the geometric area of the glassy carbon (0.196 cm^2). The mass activity and specific activity were calculated by the loading amount and ECSA of Pt, respectively. The ADTs were performed by cyclic potential sweeps under the potential range between 0.6 and 1.1 V *versus* RHE at a scan rate of 100 mV/s. During the long-term ADTs, graphite rod and O_2 was used as reference electrode and gas atmosphere, respectively.

2.3. TEM investigation

TEM imaging was performed using a JEM-2100 (JEOL, Japan) microscope equipped with an Oxford Instruments EDS detector at 200 kV. Particle size distributions were estimated through the measurement of 100 particles.

2.4. STEM and EDS investigations

ABF and HAADF-STEM results were acquired on probe-corrected (CEOS) JEM ARM 200CF (JEOL, Japan) at the Beamline E01 in the electron Physics Science Imaging Center (ePSIC). The STEM is equipped with large solid-angle dual EDS detectors for X-ray spectroscopy and elemental mapping. High resolution aberration-corrected ABF and HAADF-STEM images were acquired with an accelerating voltage of 200 kV. The probe current was 143 pA (5C probe size) with a 40 μm probe-forming aperture, resulting in 31.8 mrad probe convergence semi-angle. The HAADF signal was gathered at 4.0 cm STEM camera length, integrating the scattered electron intensity between 107.0 and 415.1 mrad. Energy-dispersive X-ray spectroscopy (EDS) data were obtained in STEM mode with the same parameters. Each EDS spectrum image is 100 × 100 pixels in size, with 0.1 s exposure time per pixel and drifting correction. Gatan Microscopy Suite Software was used for EDS spectrum imaging data acquisition, energy calibration and EDS data mapping.

2.5. Ex situ and in situ X-ray absorption spectroscopy investigations

X-ray absorption near edge structure (XANES) and extended X-ray absorption fine structure (EXAFS) of the Pt L_3-edge (11.564 keV) and Pd K-edge (24.350 keV) were performed at 3.0 GeV with a beam current of 300 mA at the Beamline B18 of

the Diamond Light Source [43,44]. For Pt L_3-edge measurement, a QXAFS setup was applied using a fast-scanning Si (1 1 1) double crystal monochromator (DCM) and a Cr-coated branch of collimating and focus mirrors (OH mirrors). Si (3 1 1) DCM and Pt-coated OH mirrors were instead used for Pd K-edge measurement. The typical photon flux at 8 keV was 5×10^{11} ph/s with a beam size of 200(H) × 250 (V) μm. The time resolution of the spectra was 3.0 min/spectrum. The energy range for Pt L_3-edge (0.3 eV/step) and Pd K-edge (0.5 eV/step) were 11.364–12.364 keV and 24.150–25.250 keV, respectively.

Ex situ XANES and EXAFS measurements were performed in both transmission mode using ion chamber detectors and fluorescence mode using a 36-element Ge solid-state detector. Pt and Pd foil were used for energy shift calibration. PtO_2 and PdO were diluted with boron nitride and pressed into 8-mm diameter pellets for transmission measurement as references. The *in situ* XANES and EXAFS of PtPd/C and commercial Pt/C were performed in a self-designed three-electrode liquid cell (Fig. S28) with same X-ray beam set-up and data acquisition parameters.

The *in situ* electrochemical cell in fluorescence mode was equipped with a three-electrode system (Fig. S28). The as-prepared carbon electrode was used as the working electrode and is sealed on the wall by Kapton foil and then a stainless-steel current collector. The cell was filled with electrolyte (0.1 M $HClO_4$) with Pt wire and Ag/AgCl electrodes-soaked in. Before *in situ* experiment, few CV cycles were run to remove any impurities and oxidized species on sample surface. The cell was placed 45° to X-ray beam direction, and the Ge detector was positioned from vertical direction to measure the fluorescence X-ray (Fig. S28C).

For the sample preparation, the catalysts were dispersed in the mixture containing ethanol and Nafion (0.005 wt% Nafion), and the concentration of the prepared ink solution was 2 $mg_{catalyst}$/ml. The ink solution was then sprayed on a conductive carbon paper as free-standing support and diffusion media (area 1 cm^2, Sigracet 29 AA, fuel cell store). The catalyst loading was controlled in a range of 0.4 to 1.5 mg/cm^2.

The PdPt/C catalysts were studied at both Pt L_3-edge and Pd K-edge, and commercial Pt/C catalysts were studied at the Pt L_3-edge as comparison. The *in situ* experiments for each sample contained two stages. First, cyclic voltammetry with very slow scanning rate (2 mV/s) was taken under the potential range of −0.225 to 1.05 V vs Ag/AgCl. In the second stage, chronoamperometric measurement was taken under onset potential, half-wave potential and limiting current potential. XAFS spectra were continuously collected during both processes. *Ex situ* XAFS data for these *in situ* samples were also performed in transmission mode before mounted into the *in situ* cell.

XAFS data analysis was performed by Demeter software package (including Athena and Artemis, version 0.9.26) [45]. Athena was used for energy calibration, data normalization and Linear Combination Fitting (LCF) analysis. Artemis was used to fit the Fourier-transformed EXAFS data (fit range: 3.2 $Å^{-1} < k < 12.1$ $Å^{-1}$ and 1.0 Å < R < 3.3 Å). The amplitude reduction factor S_0^2 was calculated to be 0.75 and 0.80 for Pt L_3-edge and Pd K-edge from the EXAFS analysis of Pt foil and Pd foil. S_0^2 was used as a fixed parameter for EXAFS data fitting. Self-absorption effect for both Pt L_3-edge and Pd K-edge was evaluated by comparing transmission and fluorescence EXAFS of the same sample. The coordination numbers fitted from transmission and fluorescence data are the same, indicating that the self-absorption effect was negligible.

XANES at Pt L_3-edge region was also analysed by the Δμ-technique developed by Ramaker et al. [46-49]. Δμ results of normalised XANES were obtained by subtracting the XANES at 0.58 V in anodic scan (vs RHE). E_0 values for all XANES spectra were set to 11564 eV. Normalisation (order = 2) was carried out between 50 and 200 eV relative to E_0. Δμ analysis provides solid evidence on different oxygen binding sites (atop O/Pt and n-fold O/Pt), as well as quantitatively probes the changes of these species under reaction conditions.

2.6. IL-EM investigations

For the IL-TEM/STEM measurements, a gold finder grid, loaded with PdPt/C catalyst, is attached to the working electrode (Fig. S26 A, B). Before any electrochemical measurement, a series of TEM images at different magnifications were recorded to locate the certain particles. The locations of target areas were tracked using the abecedarian on the gold finder girds [50] (Fig. S26 C). After different cycles of accelerated durability tests (ADT), the gird was removed from glassy carbon disc, rinsed carefully with deionized water, dried thoroughly, and then transferred to the TEM/STEM again. Energy-Dispersive X-ray Spectroscopy (EDS) data were obtained in STEM mode with the same parameters. Each EDS spectrum image is 120 × 120 pixels in size, with 0.1 or 0.05 s exposure time per pixel and drifting correction. The EDS maps of IL-STEM samples at different cycles were collected using the same magnification, sample rotation, scan range and step size. The interference of different beam current during each measurement are considered as constant. The counts values in all channels are calibrated by pixel time. Elementary maps of Pd Lα signals and Pt Lα signals are generated with background noise removed. For Pt Lα signals, the overlapped Au Lα signals are subtracted using peak fitting. The EDS maps from different cycles are aligned and cropped to 100 × 100 pixels. To improve the signal to noise ratio, a down sampling process by merging 4 × 4 pixels for each image, leading to resolution drop from 100 × 100 pixels to 25 × 25 pixels. Plot of Pd:Pt signal ratios are generated from Pd EDS image divided by Pt EDS image (pixels at the empty region with values of zero are excluded).

2.7. PXRD investigations

PXRD measurements were performed using a StadiP diffractometer from STOE, with a voltage of 40 kV and a current of 30 mA, using a Cu source with $K\alpha_1$ = 1.540562 Å and $K\alpha_2$ = 1.544 398 Å. The signal from $K\alpha_2$ was removed for analysis.

2.8. XPS investigations

XPS analyses were performed on an XPS Kα surface analysis machine (Thermoscientific) using an Al source (excitation energy at 1486.6 eV).

2.9. MP-AES investigations

The concentration of the catalysts was determined by microwave plasma-atomic emission spectrometer (4100 MP-AES). Commercial H_2PtCl_6 and $PdCl_2$ standard solution for AES and AAS were used for calibration of concentration.

2.10. Computational methods

The periodic density functional theory (DFT) calculations were performed using the Vienna *ab initio* Simulation Package (VASP) version 5.4.1 [51], which solves Kohn-Sham equations in an iterative manner [52]. Interactions between core and valence electrons were modeled with the projector augmented wave (PAW) method [53,54], and the kinetic energy cutoff was set to 400 eV. All calculations were performed under the generalized gradient approximation (GGA), and exchange and correlation effects were treated using the PBE exchange-correlation functional [55]. To model the

low-index PdPt (111) surfaces, a five-layer p(3 × 3) slab was employed, whose two bottom-most layers were fixed, while the three top-most layers were allowed to fully relax during ionic optimization. Periodic images on the *z*-direction were separated by a vacuum region of thickness of 10 Å. The corresponding lattice constants of Pt and Pd were found equal to 3.943 Å and 3.977 Å, respectively. Furthermore, the lattice constant of the investigated Pt/Pd alloy surfaces were determined based on a linear relationship, which allowed us to correlate the lattice constant of the alloy to the Pt and Pd loadings therein (Fig. S29). The Brillouin zone was sampled with a 4 × 4 × 1 Monkhorst-Pack *k*-point mesh, while the Hellman-Feynman forces acting on all ions that are free to move were relaxed to<10^{-2} eV/Å. The number of k-points was chosen after converging the adsorption energy of atomic O on a Pt/Pd (111) surface with respect to the *k*-point mesh (Supplementary Fig. S30), and the average adsorption energy of *n* O atoms (E_{ads} (*n*·O)) was computed using the following expression:

$$E_{ads}(n\cdot O) = \frac{\left(E_{tot}^{n\cdot O+slab} - E_{tot}^{slab} - n\cdot\left(E_{tot}^{O_{2(g)}}/2\right)\right)}{n} \quad (1)$$

where $E_{tot}^{n\cdot O+slab}$ is the DFT energy of *n* O atoms co-adsorbed on slab, $E_{tot}^{slab}$is the DFT total energy of the clean slab and $E_{tot}^{O_{2(g)}}$ is the DFT total energy of an O_2 molecule in the gas phase. According to the definition of E_{ads} (*n*·O)) in (Eq. S1), more negative E_{ads} (*n*·O)) values indicate stronger O binding on the catalytic surface. Finally, the *d*-projected density of states (DOS) of the two top-most layers of some of the investigated alloy surfaces were calculated using LOBSTER version 3.2.0 [56-58]. The *d*-band center of the obtained *d*-states surfaces was computed as the first moment of the *d* DOS [59].

3. Results and discussion

3.1. Design of porous PdPt/C alloy

PdPt/C alloy particles are prepared via seed-mediated methods to achieve high activity and stability.[60] Pd seeds are firstly loaded onto the conductive carbon support, followed by controlled growth of PdPt alloy nano-branches (**Fig. S1**). The obtained PdPt alloy particles have a narrow size distribution of 91 ± 20 nm (**Fig. S2**) and featured with highly porous structure. As showed in TEM and HAADF-STEM images (Fig. 1**a, 1b**), each PdPt alloy particle is composed of small nanocrystals and branches (about 2 nm size) that connected together in the same orientation (Fig. 1**c** and **Fig. S3**), forming only one type of electron diffraction pattern (Fig. 1**d** and **Fig. S4**). The porous nature of the PdPt particle significantly improves the surface area. Despite 30 times larger size of PdPt to that of commercial Pt/C, a similar electrochemical surface area (ECSA) of 69 $m^2\cdot g_{metal}^{-1}$ (including both Pd and Pt) is achieved to that of commercial one (74 $m^2\cdot g_{Pt}^{-1}$, Fig. 1**g, Table S1**). Such porous feature provides larger active surface for the O_2 adsorption and reduction that solid nanoparticles, which is beneficial to high ORR performance [7,10,28]. In addition, this unique porous structure can be considered as ordered pre-assembled ultra-small nanoparticles in a narrow spherical space, in which nanoparticle movement, agglomeration and Ostwald ripening can be significantly inhibited. Moreover, compared with colloidal PdPt nanoparticles grown without the carbon (**Fig. S5**), and the individual PdPt particle branches adapt the carbon support, maximizing the metal/carbon interface (**Fig. S5**). As a result, those inserted branches can prevent the PdPt porous particles from detachment, which is a common issue for small nanoparticles.

Despite a trace amount of Pt(II) and Pd(II) that are probed by XPS on the surface of the alloy (**Fig. S6**), Pt(0) and Pd(0) are dominant in bulk, as confirmed in both Pt L_3-edge and Pd K-edge XANES

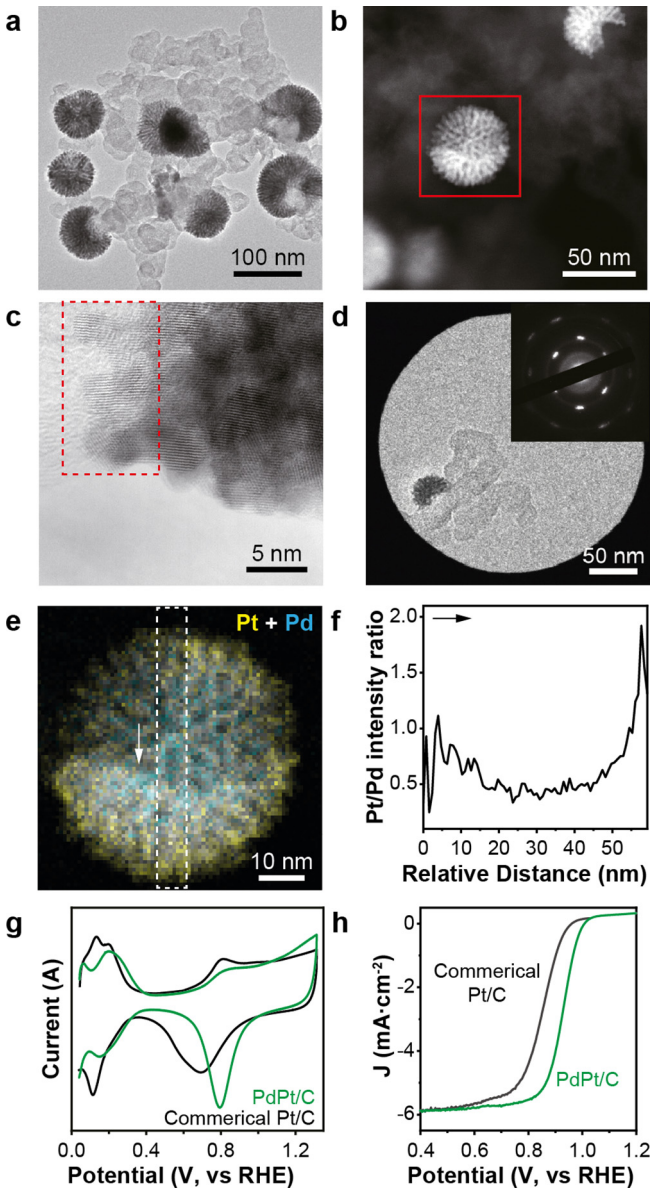

Fig. 1. Structure and ORR performance of PdPt/C alloy. a) TEM image of PdPt/C nanoparticles supported on conductive carbon. b) HAADF-STEM image of a single PdPt/C particle. c) ABF-STEM image showing the insertion of metal branches into carbon. d) Selected area electron diffraction of a single PdPt/C particle. e) STEM-EDS element mapping of particle in b). f) Pt/Pd EDS signal intensity ratio cross the vertical direction in e). g) CV curve of PdPt/C and commercial Pt/C with the same metal loading of 27 μg·cm^{-2}. h) Linear sweep voltammetry (LSV) curves of the PdPt/C alloy and commercial Pt/C.

(**Fig. S7**). Further EXAFS analysis reveals the coordination environment of Pt and Pd. First, the coordination numbers (C. N.) of Pt-Pt, Pt-Pd, Pd-Pt and Pd-Pd scatterings are 6.03 ± 0.3, 4.09 ± 0.2, 3.81 ± 0.3, and 6.67 ± 0.3, respectively (**Fig. S8, S9** and **Table S2**). The C.N. of Pt-Pt and Pd-Pd are larger than those of Pt-Pd and Pd-Pt, suggesting partial segregation of the two metals in the PdPt nanoparticle. This is in good agreement with the energy dispersive X-ray spectroscopy (EDS) mapping, where both Pd and Pt are found to be uniformly dispersed throughout the particle (Fig. 1**e**) but Pt/Pd EDS intensity ratio is higher at the peripheral part than that in the centre (Fig. 1**f** and **Fig. S10**). Second, the total C.N. for Pt-metal and Pd-metal are 10.12 and 10.48, which are smaller than the Pt and Pd foil (C. N. = 12). This result suggests the nanocrystal nature of the PdPt/C alloy. Third, the bond lengths are 2.73 ± 0.01 Å, 2.7

3 ± 0.01 Å, 2.73 ± 0.01 Å, 2.74 ± 0.01 Å for Pt-Pt, Pt-Pd, Pd-Pt and Pd-Pd, respectively, matching the values for Pt and Pd foil standards. Due to the same crystalline structure in Fm $\bar{3}$ m space group with 0.03% lattice mismatch, the PdPt/C alloy has the same sets of diffraction peaks in the X-ray diffraction (XRD), corresponding to the Pt standard and Pd standard (**Fig. S11**). Benefiting from this porous metallic PdPt/C alloy structure, the ORR mass activity of PdPt/C is 0.82 A·mg_{Pt}^{-1} compared to only 0.13 A·mg_{Pt}^{-1} for the commercial Pt/C catalyst. This also leads to high specific activity of 0.67 mA·cm^{-2} for total metal loading, which is four times higher than that of commercial Pt/C. The mass activities and ECSA for Pt and metal loadings are surmised in **Table S1** for further comparison.

3.2. Structure evolution of PdPt/C alloy in ORR condition

To further understand the high specific ORR activity of the PdPt/C alloy catalysts, the electronic and geometric structure of bulk Pt and Pd is studied *via in situ* XANES and EXAFS along with the cyclic voltammetry (CV) scan (Fig. 2**a and 2b**), probing the dynamic changes of oxidation states and Pt-O, Pt-M coordination (Fig. 2**a to 2 h**, **Fig. S12, S13, Table S3, S4 and S5**). On the one hand, Pt (0) is oxidized to PtO_x in the anodic scan and is reduced back to Pt (0) in the cathodic scan for both PdPt/C and commercial Pt/C. This redox of Pt is associated with the change of Pt oxidation states (Fig. 2**c and 2d**), the increase and decrease of Pt-O C. N. (Fig. 2**e, 2f**), as well as the decrease and increase of Pt-Pt/Pd C. N. (Fig. 2**g, 2h**). Meanwhile, the PtO_x content in the cathodic scan is maximized around 1.1 V vs. reversible hydrogen electrode (RHE) (Fig. 2**c, 2d**). This suggests that a high activation barrier is required for the reduction of PtO_x in both catalysts. On the other hand, the degrees of Pt redox are different in PdPt/C and commercial Pt/C. First, as revealed by the trend of Pt(IV) content and Pt-O C.N., amount of PtO_x formed in PdPt/C is approximately half of that in commercial Pt/C at same potential during the whole CV scan. This suggests that PdPt/C maintains more metallic feature than commercial ones. Second, in the anodic scan, significant oxidation of Pt in PdPt/C is only observed between 1.0 V and 1.1 V (vs RHE), while PtO_x started between 0.9 V and 1.0 V (vs RHE) for commercial Pt/C. At 1.0 V, the oxidation current of PdPt/C is 0.16mAh/mg_{meta}, which lower than that of commercial Pt/C (0.38 mAh/mg_{metal}). This result further approve that PdPt/C is more difficult to be oxidized than commercial Pt/C. Correspondingly, in cathodic scan, 0.1 V less potential is required for full reduction of PtO_x in PdPt/C than in commercial Pt/C. Such differences of the redox threshold potentials indicate an improved oxidation resistance of Pt in PdPt/C alloy. Third, oxidation of Pt in PdPt/C alloy at high potentials results in decrease of both Pt-Pd and Pt-Pt C.N., and the C.N. ratio between Pt-Pd and Pt-Pt remained almost the same (Pt-Pd: Pt-Pt = 0.7). Pd (II) content is detected at higher potential than Pt due to easy dissolution of oxidized Pd content in acidic electrolyte, which can't be detected by XAFS (**Fig. S14**). Therefore, it is concluded that oxygen adsorption and insertion and reduction are mainly happened at Pt sites.

The formation of PtO_x shows the O has penetrated into the sublayers of Pt lattices, which consequently changes the surface O adsorption behaviour. XANES difference spectra is then analysed by the $\Delta\mu$-technique to probe the adsorbed oxygen species (denoted as O/Pt) at the Pt surface [46-49]. In our case, $\Delta\mu$ is calculated *via* $\Delta\mu = \mu(O/Pt) - \mu(Pt)$, in which the $\mu(O/Pt)$ and $\mu(Pt)$ represent the XANES of Pt with surface oxygen species and 'clean' surface respectively. The Pt L_3-edge XANES at 0.58 V in the anodic scan is chosen as the reference spectra because this surface is free of adsorbed H, OH, O or ClO_4^- species (double layer region) [46]. The $\Delta\mu$ spectra cancels out the contribution from unchanged bulk,

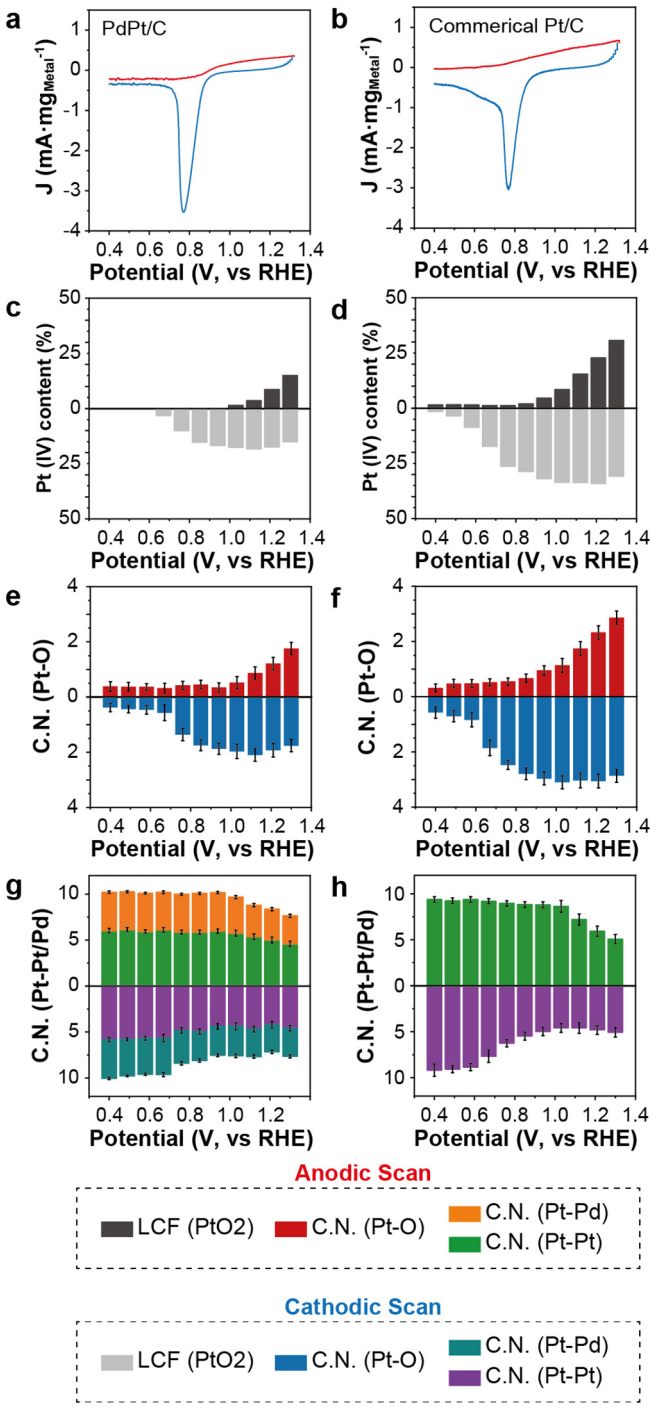

Fig. 2. *In situ* XAFS fitting results at Pt L_3-edge for PdPt/C and commercial Pt/C catalysts. CV curves of a) PdPt/C alloy and b) commercial Pt/C during *in situ* XAFS study. Change of Pt(IV) content (%) in c) PdPt/C alloy and d) commercial Pt/C as a function of electrochemical potentials (Black: anodic scan; Grey: cathodic scan). The Pt(IV) ratio is quantified by Linear Combination Fitting (LCF) of Pt L_3-edge XANES spectra. The XANES spectra has been normalized to absorption of 1 after the absorption edge (**Table S3**). Change of Pt-O coordination numbers (Blue: anodic scan; Red: cathodic scan) in e) PdPt/C alloy and f) commercial Pt/C as a function of electrochemical potentials. g) Change of Pt-Pt (Green: anodic scan; Purple: cathodic scan) and Pt-Pd coordination numbers (Orange: anodic scan; Teal: cathodic scan) in PdPt/C alloy and h) change of Pt-Pt (Green: anodic scan; Purple: cathodic scan) coordination numbers in commercial Pt/C as a function of electrochemical potentials. Cathodic scans (lower chart) are reversed to show the difference to the anodic scans (upper chart). Coordination numbers of Pt-O, Pt-Pd and Pt-Pt are determined by EXAFS fitting (**Table S4, S5**). Before *in situ* experiment, few CV cycles were run to remove any impurities and oxidized species on sample surface. (For interpretation of the references to color in this figure legend, the reader is referred to the web version of this article.)

therefore the effects from surface species such as adsorbates can be isolated with more prominent features [46-49].

The processed $\Delta\mu$ results (Fig. 3) unravel the different evolution pathways of surface oxygen species in PdPt/C and commercial Pt/C catalysts. The surface oxygen species can be classified into 1-fold atop and *n*-fold (*n* = 2, 3 and 4) depending on the location of the oxygen atoms (Fig. 3**a-d**) [46-48,61-63]. They represent adsorbed O on Pt surface (1-fold atop site, can also be OH species) and the O insertion into the lattice (n-fold sites), respectively. The energy position of 1-fold atop site over PdPt alloy (denoted as atop O/PdPt) is at −1.0 eV (rel. edge, Fig. 3**c**)), which is slightly lower than that on pure Pt surface (denoted as atop O/Pt_{Pt}) at 0.0 eV (rel. edge, Fig. 3**d**). This is typical for alloy surface according to literature [48,61,64-66]. Such 1-fold atop site represent the surface O adsorption, which is highly relevant towards ORR activity [46-48,62,63]. Solvation from H_2O and H_3O^+ may help stabilize those atop O species. In comparison, $\Delta\mu$ peaks at above 2.0 eV (rel. edge) in both PdPt/C and commercial Pt/C are attributed to the *n*-fold sites (denoted as *n*-fold O/PdPt and *n*-fold O/Pt_{Pt}. This indicates the penetration of O into Pt lattice and formation of PtO_x, which leads to limited adsorption and conversion of O_2. The formation of O in Pt lattice is coexisting with the Pt oxidation, suggesting a potential relation between these two spectroscopic features.

During the CV scan, the content of 1-fold or n-fold species and their energy position are plotted as the function of potential (Fig. 3**e, 3f**). The atop O/PdPt species keeps at −1.0 eV (rel. edge) in both anodic (0.67–1.03 V) and cathodic scan (0.76–0.13 V). The atop O/Pt_{Pt} species is absent in anodic scan and is only visible below 0.4 V (vs RHE) in cathodic scan. At the PdPt surface, both the 1-fold atop and n-folds sites are well distinguished with fixed energy position. This is not the case at the Pt surface, where a dynamic change of the $\Delta\mu_{max}$ energy position is observed. In addition, the full conversion from 1-fold atop to n-fold species at PdPt surface requires 1.12 V and the reduction back to 1-fold atop is observed at 0.76 V. The potentials required for commercial Pt are 0.67 V for oxidation and 0.40 V for reduction, respectively, suggesting that surface Pt in the PdPt is more resistant to oxidation. This result corresponds well with the CV (Fig. 1**g**), LSV (Fig. 1**h**), and the XAFS analysis (Fig. 2). The distinct atop O/PdPt species and the resistance towards oxidation can be understood that during the chemical adsorption of O at Pt surface, neighbour Pd atoms donate electrons while the Pt atoms keep at metallic state. Especially, at ORR relevant potentials between 0.7 and 0.9 V, PdPt/C mainly contains the adsorbed atop O/PdPt species whereas the commercial Pt/C possess mainly PtO_x with sublayer/lattice oxygen features.

In summary, Pd in PdPt/C catalysts plays crucial role by promoting adsorption of surface atop O/PdPt species, preventing insertion of oxygen into Pt lattice and enhancing release of PtO_x lattice oxygen. Consequently, less structural changes of PdPt/C are expected compared to commercial Pt/C at same reaction conditions, and the improved oxidation resistance of PdPt/C is fundamental to higher stability and longer lifetime than commercial Pt/C.

3.3. Structure evolution of PdPt/C at single particle level in ADT

It is confirmed by XAFS and Δμ analysis that the presence of Pd in the subsurface layer of PdPt alloy enables formation of atop O/PdPt species and improves the stability by keeping Pt at the metallic phase. In addition to this, the role of Pd played in long-term catalyst stability is further investigated by ADT. In the ADT between 0.6 and 1.1 V (vs RHE), there is only 1% MA decay till 20,000 cycles (**Fig. S15**), before being slightly reduced to 88% of the original mass activity at 30,000 cycles (Fig. 4**a, 4b**). From this point onwards, the mass activity drops steadily to 48% at 60,000 cycles (Fig. 4**b, Fig. S15**), indicating a two-stage decay mechanism. In comparison, the stability of commercial Pt/C catalysts has been widely studied, which shows less than half of initial activity within 5,000 cycles [19,67,68]. The non-porous PdPt nanoparticles, as reported previously, also suffers from poor stability with 12% of mass activity decay in the first 5,000 cycles [69,70].

To understand the drop of activity after 30,000 cycles, IL-STEM study is performed for particles at 10,000, 30,000 and 45,000 cycles, showing that the observed porous PdPt alloy particles remain in the same location and have almost the same size and morphology during ADT (Fig. 4**c to 4q** and **Fig. S16**). Additionally, IL-TEM images are also acquired at two separate areas for PdPt particles after 0, 5000, 15,000, and 20,000 ADT cycles, in which 40 of 44 and 21 of 21 particles remain at the same location in each area (**Fig. S17**). In comparison, the growth, aggregation and detachment of small Pt particles during ADT at the first 10,000 cycles is widely reported in the literature [33,40]. Therefore, the PdPt/C catalyst exhibits excellent geometric stability against detachment, agglomeration and Ostwald ripening by gripping large porous PdPt particles onto the carbon framework. Then on this basis, the element leaching can be decoupled from these deactivation pathways, as well as its effect towards decay of ORR activity in the ADT can be studied accurately.

During ADT from 10,000 to 45,000 cycles, the lattice fringes of PdPt particle show no major changes (**Fig. S18**), and the size of nano-branches in the identical PdPt nanoparticles remain almost the same (**Fig. S19**). But a drop of HAADF-STEM signal intensity at the peripherical part can be observed (Fig. 4**d, 4i, 4n** and **Fig. S20**). The result suggests that leaching starts at the PdPt/electrolyte interface, while the PdPt/C interface remains intact. Based on the IL-STEM study, the quantitative description of Pd and Pt loss is further provided by IL-EDS mapping at single-particle level, showing the similar decrease of Pd and Pt signals at the peripheral part (Fig. 4**e-g, 4j-l, 4o-q**). Furthermore, the dissolution behaviour for Pd and Pt is different: In the first stage from 10,000 to 30,000 ADT cycles, the drop of peripheral Pd intensity (Fig. 4**f and 4k**) is much faster than the observed drop of peripheral Pt intensity (Fig. 4**e and 4j**); In the second stage from 30,000 to 45,000 cycles, there is no clear Pd leaching in the particle (Fig. 4**k and 4p**), while Pt undergoes severe leaching (Fig. 4**j and 4o**). Similar leaching behaviour is also confirmed by IL-EDS study of another PdPt particle at 10,000, 30,000 and 45,000 ADT cycles (**Fig. S20**). This trend is clearly visualised in the plot of Pd:Pt signal ratio, showing that Pd:Pt ratio dropped during 10,000 to 30,000 ADT cycles (Pd dominant leaching) and increased after 45,000 ADT cycles (Pt dominant leaching) (Fig. 4**g, l, q**).

Here, the initial leaching of Pd is in good agreement with the reports in Pt-based alloy system, in which the less noble alloy components are always preferentially leached during electrochemical potential cycling [71-73]. This is due to their low reduction potentials in comparison with Pt. With less Pd, the PdPt has a higher tendency of oxidation according to the comparison between PdPt and Pt in the *in situ* XAFS study (Figs. 2, 3). The absent of Pd after 30,000 ADT cycles eventually causes the Pt leaching between 30,000 and 45,000 ADT cycles *via* fast redox between metallic and oxidation states. The change of Pd and Pt content in the alloy explains the change of ORR mass activity, which is steady till 30,000 cycles and then decreases between 30,000 and 45,000 cycles (Fig. 4**b, Fig. S15**).

3.4. DFT calculation based on single-particle imaging

To rationalize the observed trend of mass activity during the ADT experiment (Fig. 4**a and 4b**), periodic DFT calculations are performed based on the results from the IL-STEM study (Fig. 4**c to 4q**), which also enables the correlation between the measured mass activity and the structural evolution of the PdPt/C catalyst during

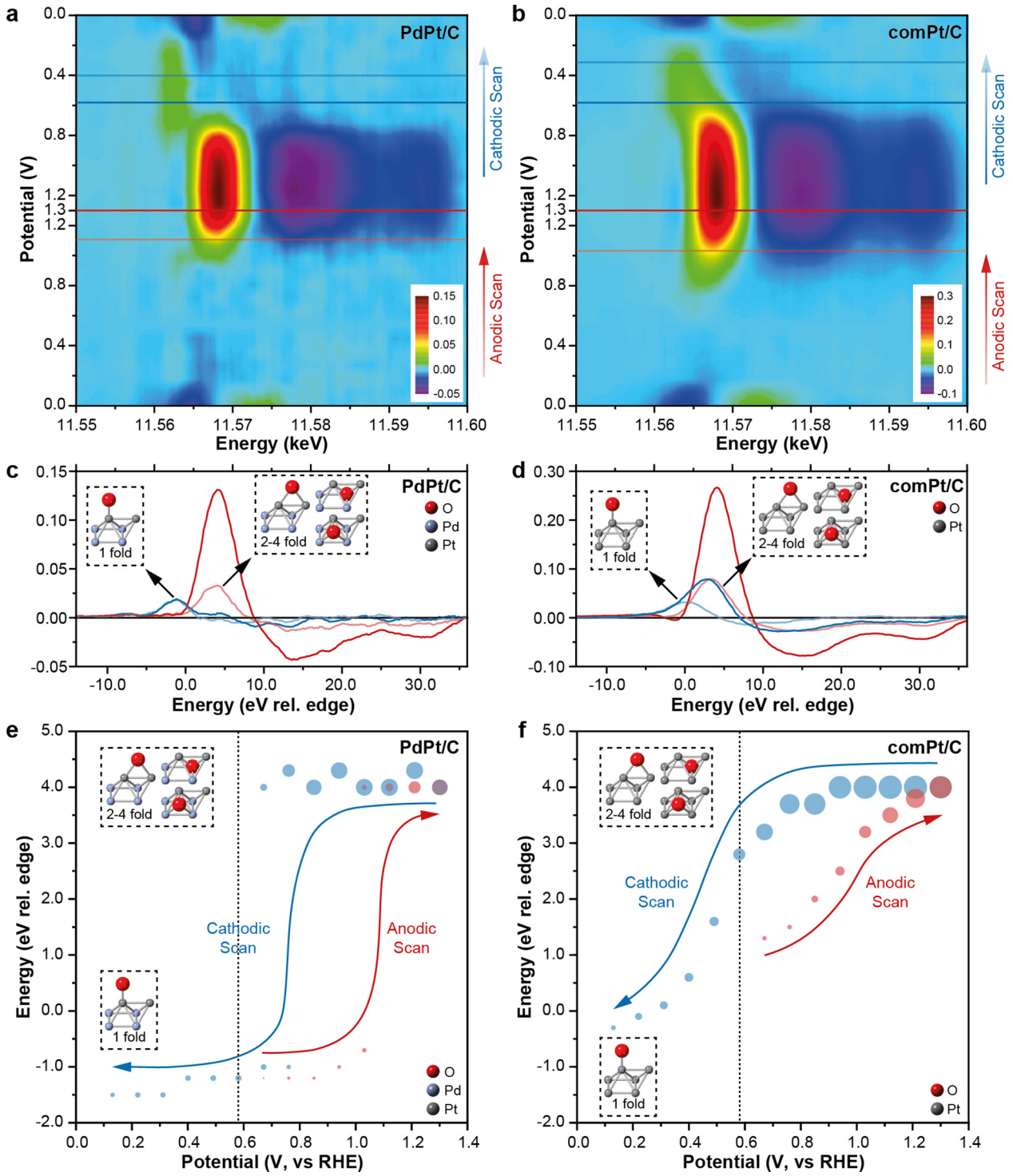

Fig. 3. $\Delta\mu$-analysis of *in situ* XANES at Pt L_3-edge for PdPt/C and commercial Pt/C catalysts. Heatmaps of $\Delta\mu$ results of a) PdPt/C and b) commercial Pt/C as function of potential during CV scan. The potential range of CV scan is 0.0 to 1.3 V (vs. RHE). The color bar with magnitude is attached. c) $\Delta\mu$ magnitudes for PdPt/C catalysts at 1.12 V (light red curve) and 1.30 V (dark red curve) in anodic scan, as well as 0.58 V (dark blue curve) and 0.40 V (light blue curve) in cathodic scan. The edge position is fixed at 11564 eV. d) $\Delta\mu$ magnitudes for commercial Pt/C catalysts at 1.03 V (light red curve) and 1.30 V (dark red curve) in anodic scan, as well as 0.58 V (dark blue curve) and 0.31 V (light blue curve) in cathodic scan. Bubble plot of $\Delta\mu_{max}$ energy for e) PdPt/C and f) commercial Pt/C as function of potential during CV scan. Data points of $\Delta\mu_{max}$ at different potentials are differentiated into red and blue bubbles, representing anodic scan and cathodic scan respectively. The area of each bubble indicates the value of each $\Delta\mu_{max}$, correspond to the amount of specific surface species. The red, blue and gray spheres in the structure illustrations in c-f represent oxygen, palladium and platinum atoms, respectively. The commercial Pt/C is the initial of commercial Pt/C. (For interpretation of the references to color in this figure legend, the reader is referred to the web version of this article.)

ORR. In more precise terms, we have computed the adsorption energy of O on a number of PdPt (111) surfaces (Fig. 5**a, 5b**). Solvation from H_2O is yet considered in the model. Due to the scaling relation between O* and OH* adoption energies, the E_{ads} O calculated here is a good descriptor of the catalytic activity [29,30]. In the calculations, the composition of the two top layers of the sur-

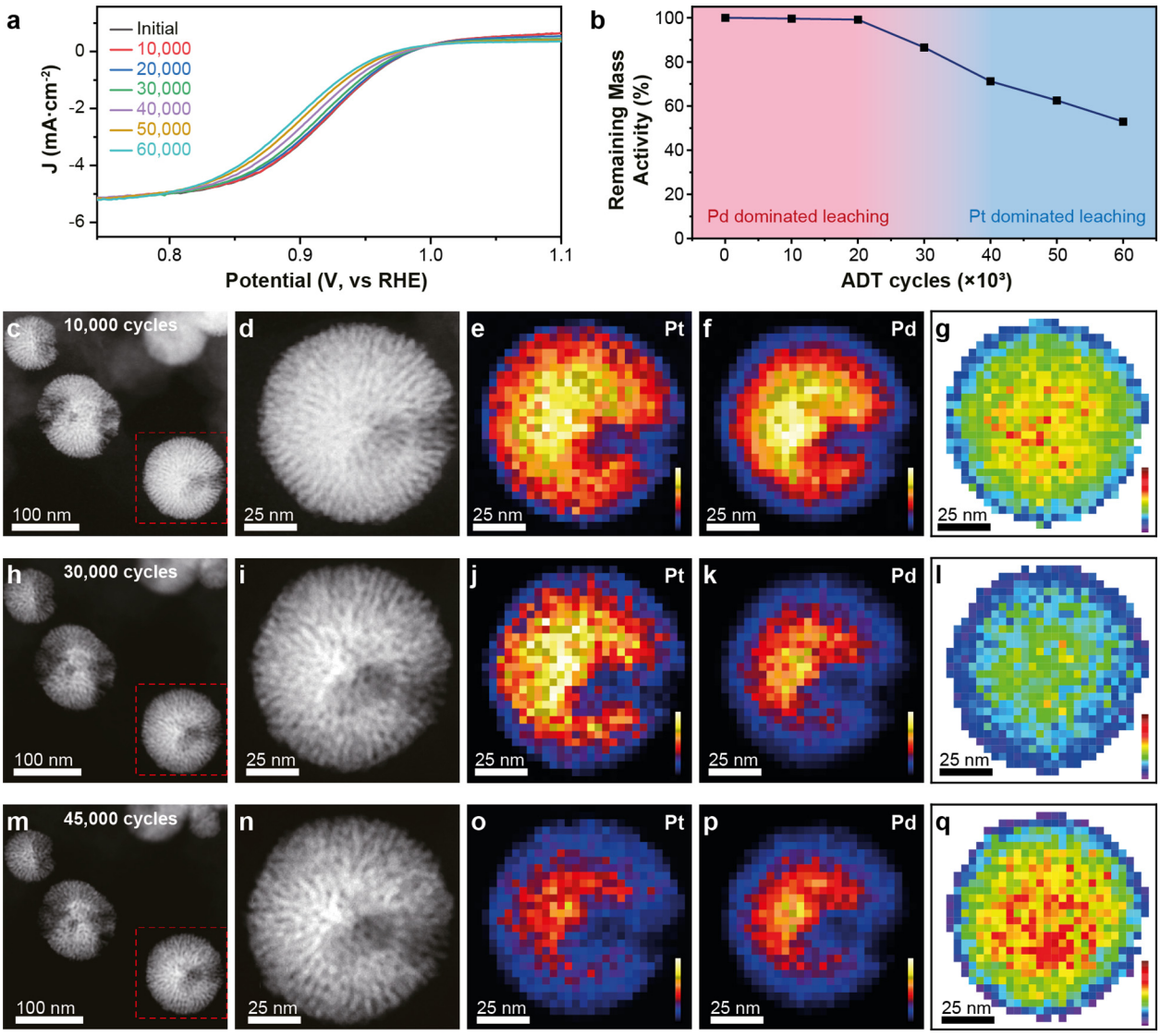

Fig. 4. Structure evolution of PdPt/C at single particle level at different ADT cycles. The ADT experiment is carried out in 0.1 M $HClO_4$ solution at a sweep rate of 100 mV/s between 0.6 and 1.1 V (vs RHE). During the long-term ADTs, graphite rod and O_2 was used as reference electrode and gas atmosphere, respectively. a) LSV curves of PdPt/C after different ADT cycles. b) Corresponding mass activity of PdPt/C after different ADT cycles. c-d) IL HAADF-STEM images, EDS element mapping of e) Pt Lα and f) Pd Lα. G) EDS signal ratio of Pd Lα to Pt Lα of a single PdPt/C alloy particle after 10,000 ADT cycles. IL HAADF-STEM images and EDS element mappings after h-l) 30,000 ADT cycles and m-q) 45,000 ADT cycles. The increase of element concentration is displayed by colour changes from purple to white. The counts values in all EDS spectrum channels are calibrated by pixel time. The increase of Pd/Pt ratio is displayed by colour changes from purple to red. Scale bar: 100 nm in c, h, m and 25 nm in d-g, h-l, m-q. (For interpretation of the references to color in this figure legend, the reader is referred to the web version of this article.)

face is varied, as the subsurface layer may still affect the O adsorption energy. We fix the composition of the three bottom layers, which, anyway, have a small effect on the binding strength of O species [74].

DFT calculations first elucidate the property of the surface oxygen over PdPt surface and the role of Pd on surface and subsurface. Those subsurface atoms can change the electronic structure of the top layer Pt and affect the O* adsorption. As shown in Fig. 5**a**, the binding strength of O on the PdPt (111) surface with a Pt skin and 33% Pt on the subsurface layer is reduced by ca. 0.04 eV per O adatom as compared to a pure Pt (111) surface (structure 4 in Fig. 5**b**). Generally, a value of $E_{ads}O$ and $E^{Pt}_{ads}O$ within the range of 0 to 0.2 eV lead to reduced barriers for O desorption, thereby increasing the ORR activity [29]. Therefore, it is the facile O desorption from the surface of the PdPt that play a key role in maintaining Pt in the metallic phase at high potential, as confirmed in the XAFS and Δμ studies above as well.

Since Pd leaching is more pronounced than Pt leaching in the first 30,000 ADT cycles (Fig. 4**f, 4k**), one may first assume a surface layer devoid of Pd. On this basis, the O adsorption is simulated on a slab with a Pt skin and a Pd subsurface layer. For this structure, the $E_{ads}O$ = −0.78 eV (structure 1 in Fig. 5**a and 5b**) is computed. In addition, the high initial Pd leaching rate will potentially cause the enrichment of the subsurface layer in Pt (structures 2, 3 and 4 in Fig. 5**a, 5b**). This will happen through Pd segregation to the surface layer followed by Pd leaching into the electrolyte. Interestingly, the DFT calculations suggest that the bespoke enrichment has a very small effect on $E_{ads}O$ (Fig. 5**a**). For example, it is found that the difference in $E_{ads}O$ between a structure with a Pt fraction of 1.0 and 0.0 on the surface and subsurface layers (structure 1 in Fig. 5**a and b**), respectively, is by only 30 meV smaller than a structure with a Pt fraction of 1.0 and 0.33 on the surface and subsurface layers (structure 4 in Fig. 5**a and b**), respectively.

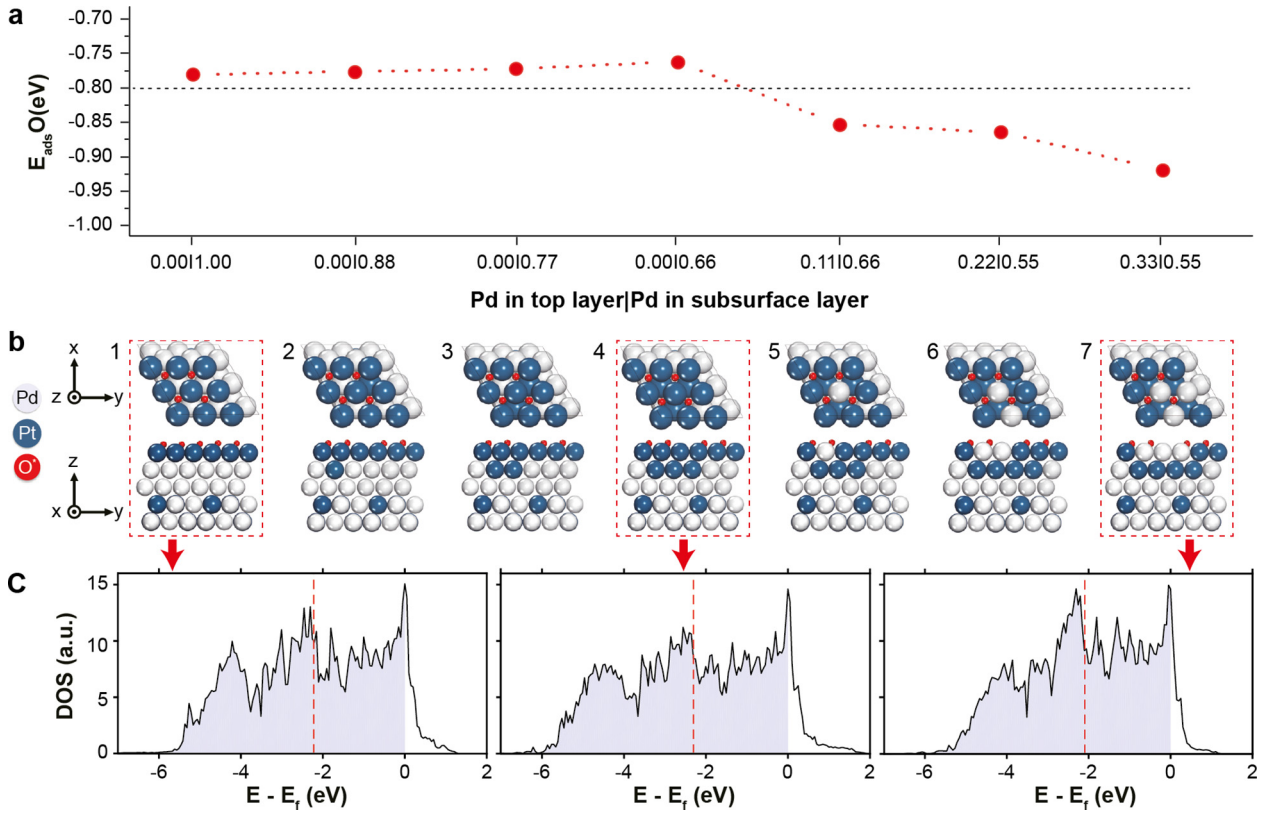

Fig. 5. DFT calculation of the Pt-O binding energy on the surface of PdPt alloy. a) Computed EadsO as a function of the fraction of Pd in the top|sub-surface layers. The O coverage was 0.44 ML for all calculations and O species were adsorbed on threefold fcc sites, which are the most stable adsorption sites on Pt (1 1 1). The fractions of Pd and Pt in the three bottom layers were 0.85 and 0.15, respectively, in all cases. b) DFT slabs whereon EadsO is computed. Each structure shown in panel b) is assigned with a number (e.g. structure 1, structure 2). Pt, Pd and O atoms are shown in blue, white and red, respectively. c) density of states projected on the two top layers of the clean slab of three highlighted structures. The vertical dashed lines indicate the calculated d-band centres. (For interpretation of the references to color in this figure legend, the reader is referred to the web version of this article.)

By contrast, after 30,000 ADT cycles, Pt leaching becomes very significant (Fig. 4**j, 4o**), and this will result in a mixed PdPt surface layer (structures 5, 6 and 7 in Fig. 5**b**). The DFT calculations show that the presence of Pd, even at a low coverage of 0.11 ML (structure 5 in Fig. 5**b**), strengthens O binding by 0.1 eV per O atom as compared to the "Pt skin" structures 1–4 of Fig. 5**a**. Moreover, at increasing surface Pd coverages, O adsorption becomes progressively more exothermic, thereby clarifying the decreasing trend of the mass activity in the Pt leaching phase (Fig. 5**a, 5b**). Additional calculations show that the presence of Pd on the surface layer of the PdPt (1 1 1) results in very strong O binding on surrounded by Pt fcc sites, which, as a result, are potentially poisoned (**Fig. S21**) [29].

To elucidate the different reactivity of the structures investigated, the *d* density of states (DOS) was calculated and projected on the two top the layers of representative structures (shown in Fig. 5**c**, along with the *d*-band centre calculated as the first moment of the *d*-DOS) [75]. Our *d* DOS analysis accounts for both surface and subsurface layers because the composition of these two layers has a strongest impact upon $E_{ads}O$. Dianat et al. [74] have shown that changes in the composition of the subsurface layer, while keeping fixed the composition of the surface layer, can bring about changes of as high as 0.13 eV in $E_{ads}O$. It is observed that the *d*-band centre of structure 7 is by 0.13 eV and 0.20 eV higher than the *d*-band centres of structures 1 and 4, respectively, explaining the lower reactivity of structure 7 (i.e. more negative $E_{ads}O$) [76,77].

3.5. Ensemble stability and evolution of PdPt/C in ADT

The IL-TEM study (Fig. 4) visualizes the stability and evolution of PdPt/C at the single-particle level. It is therefore important to verify the result with an ensemble study that probes the collective behaviours of PdPt/C. To this end, ADT of PdPt/C alloy particles loaded on carbon cloth are performed in a three-electrode cell. During the whole ADT process, the decay of mass activity followed almost the same trend as that in RDE system (Fig. 4**b, Fig. S22**). Meanwhile, the morphology of PdPt particles is maintained after 45,000 ADT cycles, which is consistent with the single-particle study. Only after 60,000 cycles the porous structure started to collapse and formed some small nanoparticles (**Fig. S23**). In addition, the ensemble Pt/Pd ratios at different stages are determined by microwave plasma-atomic emission spectroscopy (MP-AES), which is complementary to EDS analysis. It is found that the Pt:Pd ratio increased from 0.43 at the fresh state to 0.48 and 0.52 at 10,000 and 30,000 cycles respectively (**Fig. S22**) and decreased to 0.49 at 45,000 cycles. Therefore, both macroscopic and microscopic analysis confirm the same Pd dominated and Pt dominated leaching zones before and after 30,000 cycles respectively, thereby supporting the selection of the DFT geometries in Fig. 5**b**. It is also worth mention that the dynamic loss rates of Pd and Pt at different ADT stages not only change the composition but also alter the alloying degree. As revealed by XAFS study, even though most of the Pt stays at metallic states, the Pt-Pd C.N. gradually decrease with more ADT cycles, suggesting the removal of Pd from Pt (**Fig. S24, Table S6**).

On top of this, a more specific $\Delta\mu$ analysis of PdPt/C after 60,000 cycles is performed to elucidate the change of surface composition (**Fig. S25**). Interestingly, the atop O/PdPt species is not observed in either anodic or cathodic scans, while O/Pt_{Pt} species is only probed only in cathodic scan. Such behavior of O adsorption is very similar to that on the pure Pt surface in commercial Pt/C and corresponds well with the dealloying of PdPt. However, the potential required for formation of lattice inserted O species in anodic scan and full conversion to surface adsorbed O species in cathodic scan are 1.03 V and 0.58 V respectively, which is lower than that of fresh PdPt/C but still higher than that of commercial Pt/C. Despite the increased oxidation resistance by Pd even after 60,000 ADT cycles, the overall ORR performance is still limited without the atop O/PdPt species due to the segregation of surface Pt and subsurface Pd, as well as the more exothermic formation of O/Pd species with increased surface Pd coverages.

4. Conclusion

Pd enables the surface adsorbed atop O/PdPt species that is essential for the ORR activity and stability. At ORR relevant potential, O_2 is reduced in the form of the atop O/PdPt, which is enabled by low $E_{ads}O$ and the electron donating effect from Pd. The presence of Pd also makes Pt more oxidation resistance, preventing the leaching of Pt in ADT cycles. Base on such resistance, the decrease of ORR activity is correlated with the decay of PdPt alloy structure at a single particle level in combination of the DFT study, show how the change of surface Pd/Pt affect the overall ORR activity.

Data availability

Data will be made available on request.

Declaration of Competing Interest

The authors declare that they have no known competing financial interests or personal relationships that could have appeared to influence the work reported in this paper.

Acknowledgement

The project is funded by EPSRC (EP/P02467X/1 and EP/S018204/2), Royal Society (RG160661, IES\R3\170097) and the Newton International Fellowship (NF170761). We acknowledge electron Physical Science Imaging Centre at Diamond Light Source (UK) for the STEM experiment (Proposal No. EM20643, EM19318 and EM19246). We acknowledge the B18 beamline of Diamond Light Source for in situ XAFS experiment (Proposal No. SP19072, SP20629 and Energy Materials Block Allocation Group SP14239). We acknowledge the BL01B1 beamline at SPring-8 (Japan) for the in situ XAFS experiments (Proposal No. 2019B1438). The UK Catalysis Hub is kindly thanked for resources and support provided via our membership of the UK Catalysis Hub Consortium and funded by EPSRC (grants EP/K014706/2, EP/K014668/1, EP/K014854/1, EP/K014714/1 and EP/M013219/1). R.X. would like to thank the China Scholarship Council (CSC) for the PhD funding.

Appendix A. Supplementary data

Supplementary data to this article can be found online at https://doi.org/10.1016/j.jcat.2022.10.025.

References

[1] Z.W. Seh, J. Kibsgaard, C.F. Dickens, I. Chorkendorff, J.K. Norskov, T.F. Jaramillo, Science 355 (2017) eaad4998.
[2] Y. Jiao, Y. Zheng, M. Jaroniec, S.Z. Qiao, Chem. Soc. Rev. 44 (2015) 2060–2086.
[3] P. Strasser, Science 349 (2015) 379–380.
[4] A. Chen, P. Holt-Hindle, Chem. Rev. 110 (2010) 3767–3804.
[5] X.X. Wang, M.T. Swihart, G. Wu, Nat. Catal. 2 (2019) 578–589.
[6] J.Z. Li, M.J. Chen, D.A. Cullen, S. Hwang, M.Y. Wang, B.Y. Li, K.X. Liu, S. Karakalos, M. Lucero, H.G. Zhang, C. Lei, H. Xu, G.E. Sterbinsky, Z.X. Feng, D. Su, K.L. More, G.F. Wang, Z.B. Wang, G. Wu, Nat. Catal. 1 (2018) 935–945.
[7] C. Chen, Y. Kang, Z. Huo, Z. Zhu, W. Huang, H.L. Xin, J.D. Snyder, D. Li, J.A. Herron, M. Mavrikakis, M. Chi, K.L. More, Y. Li, N.M. Markovic, G.A. Somorjai, P. Yang, V.R. Stamenkovic, Science 343 (2014) 1339–1343.
[8] L. Bu, N. Zhang, S. Guo, X. Zhang, J. Li, J. Yao, T. Wu, G. Lu, J.Y. Ma, D. Su, X. Huang, Science 354 (2016) 1410–1414.
[9] A.X. Yin, X.Q. Min, Y.W. Zhang, C.H. Yan, J. Am. Chem. Soc. 133 (2011) 3816–3819.
[10] B. Lim, M. Jiang, P.H. Camargo, E.C. Cho, J. Tao, X. Lu, Y. Zhu, Y. Xia, Science 324 (2009) 1302–1305.
[11] M.C. Luo, S.J. Guo, Nat. Rev. Mater. 2 (2017) 17059.
[12] J.C. Dong, X.G. Zhang, V. Briega-Martos, X. Jin, J. Yang, S. Chen, Z.L. Yang, D.Y. Wu, J.M. Feliu, C.T. Williams, Z.Q. Tian, J.F. Li, Nat. Energy 4 (2019) 60–67.
[13] R. Chattot, O. Le Bacq, V. Beermann, S. Kuhl, J. Herranz, S. Henning, L. Kuhn, T. Asset, L. Guetaz, G. Renou, J. Drnec, P. Bordet, A. Pasturel, A. Eychmuller, T.J. Schmidt, P. Strasser, L. Dubau, F. Maillard, Nat. Mater. 17 (2018) 827–+.
[14] V.R. Stamenkovic, B.S. Mun, M. Arenz, K.J. Mayrhofer, C.A. Lucas, G. Wang, P.N. Ross, N.M. Markovic, Nat. Mater. 6 (2007) 241–247.
[15] P. Hernandez-Fernandez, F. Masini, D.N. McCarthy, C.E. Strebel, D. Friebel, D. Deiana, P. Malacrida, A. Nierhoff, A. Bodin, A.M. Wise, Nat. Chem. 6 (2014) 732.
[16] P. Strasser, S. Koh, T. Anniyev, J. Greeley, K. More, C. Yu, Z. Liu, S. Kaya, D. Nordlund, H. Ogasawara, M.F. Toney, A. Nilsson, Nat. Chem. 2 (2010) 454–460.
[17] X.Q. Huang, Z.P. Zhao, L. Cao, Y. Chen, E.B. Zhu, Z.Y. Lin, M.F. Li, A.M. Yan, A. Zettl, Y.M. Wang, X.F. Duan, T. Mueller, Y. Huang, Science 348 (2015) 1230–1234.
[18] M. Escudero-Escribano, P. Malacrida, M.H. Hansen, U.G. Vej-Hansen, A. Velazquez-Palenzuela, V. Tripkovic, J. Schiotz, J. Rossmeisl, I.E. Stephens, I. Chorkendorff, Science 352 (2016) 73–76.
[19] L. Zhang, L.T. Roling, X. Wang, M. Vara, M. Chi, J. Liu, S.I. Choi, J. Park, J.A. Herron, Z. Xie, M. Mavrikakis, Y. Xia, Science 349 (2015) 412–416.
[20] J.B. Wu, J.L. Zhang, Z.M. Peng, S.C. Yang, F.T. Wagner, H. Yang, J. Am. Chem. Soc. 132 (2010) 4984.
[21] J. Li, H.M. Yin, X.B. Li, E. Okunishi, Y.L. Shen, J. He, Z.K. Tang, W.X. Wang, E. Yucelen, C. Li, Y. Gong, L. Gu, S. Miao, L.M. Liu, J. Luo, Y. Ding, Nat. Energy 2 (2017) 17111.
[22] Z.W. Chen, M. Waje, W.Z. Li, Y.S. Yan, Angew. Chem. Int. Edit. 46 (2007) 4060–4063.
[23] X. Wang, S.I. Choi, L.T. Roling, M. Luo, C. Ma, L. Zhang, M. Chi, J. Liu, Z. Xie, J.A. Herron, M. Mavrikakis, Y. Xia, Nat. Commun. 6 (2015) 7594.
[24] K.P. Gong, D. Su, R.R. Adzic, J. Am. Chem. Soc. 132 (2010) 14364–14366.
[25] M. Li, Z. Zhao, T. Cheng, A. Fortunelli, C.Y. Chen, R. Yu, Q. Zhang, L. Gu, B.V. Merinov, Z. Lin, E. Zhu, T. Yu, Q. Jia, J. Guo, L. Zhang, W.A. Goddard 3rd, Y. Huang, X. Duan, Science 354 (2016) 1414–1419.
[26] H.Q. Li, G.Q. Sun, N. Li, S.G. Sun, D.S. Su, Q. Xin, J Phys Chem C 111 (2007) 5605–5617.
[27] Y.Z. Lu, Y.Y. Jiang, W. Chen, Nano Energy 2 (2013) 836–844.
[28] H. Ye, R.M. Crooks, J. Am. Chem. Soc. 129 (2007) 3627–3633.
[29] J. Greeley, I.E. Stephens, A.S. Bondarenko, T.P. Johansson, H.A. Hansen, T.F. Jaramillo, J. Rossmeisl, I. Chorkendorff, J.K. Norskov, Nat. Chem. 1 (2009) 552–556.
[30] A. Kulkarni, S. Siahrostami, A. Patel, J.K. Norskov, Chem. Rev. 118 (2018) 2302–2312.
[31] J. Xie, D.L. Wood, D.M. Wayne, T.A. Zawodzinski, P. Atanassov, R.L. Borup, J. Electrochem. Soc. 152 (2005) A104–A113.
[32] Z. Siroma, K. Ishii, K. Yasuda, M. Inaba, A. Tasaka, J. Power Sources 171 (2007) 524–529.
[33] J.C. Meier, C. Galeano, I. Katsounaros, A.A. Topalov, A. Kostka, F. Schuth, K.J.J. Mayrhofer, Acs. Catal. 2 (2012) 832–843.
[34] K. Yoshida, Z. Xudong, A.N. Bright, K. Saitoh, N. Tanaka, Nanotechnology 24 (2013).
[35] E. Guilminot, A. Corcella, F. Charlot, F. Maillard, M. Chatenet, J Electrochem Soc 154 (2007) B96–B105.
[36] E. Guilminot, A. Corcella, M. Chatenet, F. Maillard, F. Charlot, G. Berthome, C. Iojoiu, J.Y. Sanchez, E. Rossinot, E. Claude, J Electrochem Soc 154 (2007) B1106–B1114.
[37] C.H. Cui, L. Gan, M. Heggen, S. Rudi, P. Strasser, Nat Mater 12 (2013) 765–771.
[38] Y.Y. Shao, R. Kou, J. Wang, V.V. Viswanathan, J.H. Kwak, J. Liu, Y. Wang, Y.H. Lin, J Power Sources 185 (2008) 280–286.
[39] H. Yoshida, T. Kinumoto, Y. Iriyama, Y. Uchimoto, Z. Ogumi, ECS Trans. 11 (2007) 1321–1329.
[40] J.C. Meier, I. Katsounaros, C. Galeano, H.J. Bongard, A.A. Topalov, A. Kostka, A. Karschin, F. Schuth, K.J.J. Mayrhofer, Energ, Environ. Sci. 5 (2012) 9319–9330.
[41] T. Kwon, M. Jun, H.Y. Kim, A. Oh, J. Park, H. Baik, S.H. Joo, K. Lee, Adv. Funct. Mater. 28 (2018).
[42] L. Chong, J. Wen, J. Kubal, F.G. Sen, J. Zou, J. Greeley, M. Chan, H. Barkholtz, W. Ding, D.J. Liu, Science 362 (2018) 1276–1281.
[43] A.J. Dent, G. Cibin, S. Ramos, S.A. Parry, D. Gianolio, A.D. Smith, S.M. Scott, L. Varandas, S. Patel, M.R. Pearson, L. Hudson, N.A. Krumpa, A.S. Marsch, P.E. Robbins, J. Phys. Conf. Ser. 430 (2013) 012023-012029.

[44] A.J. Dent, G. Cibin, S. Ramos, A.D. Smith, S.M. Scott, L. Varandas, M.R. Pearson, N.A. Krumpa, C.P. Jones, P.E. Robbins, J. Phys. Conf. Ser. 190 (2009) 012039–012042.
[45] B. Ravel, M. Newville, J. Synchrotron. Radiat. 12 (2005) 537–541.
[46] A. Teliska, W.E. O'Grady, D.E. Ramaker, J. Phys. Chem. B 109 (2005) 8076–8084.
[47] C. Roth, N. Benker, T. Buhrmester, M. Mazurek, M. Loster, H. Fuess, D.C. Koningsberger, D.E. Ramaker, J. Electrochem. Soc. 127 (2005) 14607–14615.
[48] M. Teliska, V.S. Murthi, S. Mukerjee, D.E. Ramaker, J. Electrochem. Soc. 152 (2005) A2159-A2169.
[49] M. Teliska, W.E. O'Grady, D.E. Ramaker, J. Phys. Chem. B 108 (2004) 2333–2344.
[50] J.C. Meier, I. Katsounaros, C. Galeano, H.J. Bongard, A.A. Topalov, A. Kostka, A. Karschin, F. Schueth, K.J. Mayrhofer, Energy Environ. Sci. 5 (2012) 9319–9330.
[51] G. Kresse, J. Furthmüller, Comput. Mater. Sci. 6 (1996) 15–50.
[52] W. Kohn, L.J. Sham, Phys. Rev. 140 (1965) A1133.
[53] G. Kresse, D. Joubert, Phys. Rev. B 59 (1999) 1758.
[54] P.E. Blöchl, Phys. Rev. B 50 (1994) 17953.
[55] J.P. Perdew, K. Burke, M. Ernzerhof, Phys. Rev. Lett. 77 (1996) 3865.
[56] R. Dronskowski, P.E. Blöchl, J. Phys. Chem. 97 (1993) 8617–8624.
[57] V.L. Deringer, A.L. Tchougréeff, R. Dronskowski, J. Phys. Chem. A 115 (2011) 5461–5466.
[58] S. Maintz, V.L. Deringer, A.L. Tchougréeff, R. Dronskowski, J. Comput. Chem. 34 (2013) 2557–2567.
[59] J.K. Nørskov, F. Studt, F. Abild-Pedersen, T. Bligaard, Fundamental concepts in heterogeneous catalysis, John Wiley & Sons, 2014.
[60] F. Wang, C. Li, L.D. Sun, C.H. Xu, J. Wang, J.C. Yu, C.H. Yan, Angew. Chem. Int. Edit. 51 (2012) 4872–4876.
[61] D.E. Ramaker, D.C. Koningsberger, Phys. Chem. Chem. Phys. 12 (2010) 5514–5534.
[62] M. Teliska, V.S. Murthi, S. Mukerjee, D.E. Ramaker, J. Phys. Chem. C 111 (2007) 9267–9274.
[63] A. Kongkanand, J.M. Ziegelbauer, J. Phys. Chem. C 116 (2012) 3684–3693.
[64] F.J. Scott, C. Roth, D.E. Ramaker, J. Phys. Chem. C 111 (2007) 11403–11413.
[65] F.J. Scott, S. Mukerjee, D.E. Ramaker, J. Electrochem. Soc. 154 (2007) A396–A406.
[66] F.J. Scott, S. Mukerjee, D.E. Ramaker, J. Phys. Chem. C 114 (2010) 442–453.
[67] Y. Xiong, Y. Yang, F.J. DiSalvo, H.D. Abruña, J. Am. Chem. Soc. (2018) 7248–7255.
[68] C. Baldizzone, S. Mezzavilla, H.W. Carvalho, J.C. Meier, A.K. Schuppert, M. Heggen, C. Galeano, J.D. Grunwaldt, F. Schuth, K.J. Mayrhofer, Angew. Chem. Int. Edit. 53 (2014) 14250–14254.
[69] X. Deng, S. Yin, X. Wu, M. Sun, Z. Li, Z. Xie, Y. Liang, Q. Huang, Int. J. Hydrog. 44 (2019) 2752–2759.
[70] J. Kim, Y. Hong, K. Lee, J.Y. Kim, Adv. Energy Mater. 10 (2020) 2002049.
[71] G. Zhang, Z.G. Shao, W.T. Lu, F. Xie, H. Xiao, X.P. Qin, B.L. Yi, Appl. Catal. B Environ. 132 (2013) 183–194.
[72] P. Strasser, Rev Chem. Eng. 25 (2009) 255–295.
[73] W. He, H.J. Jiang, Y. Zhou, S.D. Yang, X.Z. Xue, Z.Q. Zou, X.G. Zhang, D.L. Akins, H. Yang, Carbon 50 (2012) 265–274.
[74] A. Dianat, J. Zimmermann, N. Seriani, M. Bobeth, W. Pompe, L.C. Ciacchi, Surf. Sci. 602 (2008) 876–884.
[75] A. Vojvodic, J.K. Norskov, F. Abild-Pedersen, Top. Catal. 57 (2014) 25–32.
[76] B. Hammer, J.K. Nørskov, Theoretical surface science and catalysis—calculations and concepts, Advances in Catalysis, Elsevier (2000) 71–129.
[77] B. Hammer, J.K. Norskov, Surf. Sci. 343 (1995) 211–220.